Journal of Zhejiang University-SCIENCE A (Applied Physics & Engineering) 2023 24(4):377-386
www.jzus.zju.edu.cn; www.springer.com/journal/11582
E-mail: jzus_a@zju.edu.cn

Research Article

https://doi.org/10.1631/jzus.A2200566

Coupling functional anodes with natural air-diffused cathodes enables highly efficient hydrogen peroxide electrosynthesis

Chen LING[1], Aiping LIANG[1], Chaolin LI[1,2]✉, Wenhui WANG[1]✉

[1]*School of Civil and Environmental Engineering, Harbin Institute of Technology, Shenzhen, Shenzhen 518055, China*
[2]*State Key Laboratory of Urban Water Resource and Environment, School of Environment, Harbin Institute of Technology, Harbin 150090, China*

Abstract: Electrosynthesis of hydrogen peroxide (H_2O_2) is a decentralized production method with excellent application prospects. Coupling anodes with cathodes can achieve highly efficient electrosynthesis of hydrogen peroxide. In this study, we prepared an anode for H_2O_2 electrosynthesis via the two-electron water oxidation reaction (2e-WOR) by modifying carbon fiber paper with self-assembling monolayers. In addition, a natural air-diffused cathode loaded with polytetrafluoroethylene/carbon black using carbon cloth as substrate was prepared to combine with the modified anode to produce H_2O_2 simultaneously. The total current efficiency of the anode and cathode reached 152.9%, and the H_2O_2 production rate was as high as 38 μmol/min at 2.8 V vs. reversible hydrogen electrodes (RHE) in a Nafion 117 membrane-separated electrolyzer. This work reported a novel carbon-based 2e-WOR catalyst and laid a theoretical foundation for the simultaneous electrosynthesis of H_2O_2 with an anode and cathode.

Key words: Two-electron water oxidation; Two-electron oxygen reduction; Self-assembled membrane; Hydrogen peroxide; Electrosynthesis

1 Introduction

Hydrogen peroxide (H_2O_2) is a versatile 'green' oxidant widely used in industrial bleaching (Hage and Lienke, 2006), wastewater treatment (Kosaka et al., 2001), chemical synthesis (Tanev et al., 1994), and fuel cell technology (Ma et al., 2010). Global demand for H_2O_2 is expected to reach 5.2 billion USD by 2026 at an annual growth rate of 5.5% (Gopakumar et al., 2022). At present, highly concentrated H_2O_2 is produced mainly via the anthraquinone cycle process. However, the process is energy intensive with a complicated separation and purification procedure for H_2O_2 products. This requires large-scale infrastructure and poses risks during transportation and storage (Samanta and Choudhary, 2007; Edwards and Hutchings, 2008; Li et al., 2020). Decentralized production of H_2O_2 is attractive because it avoids such risks. Direct synthesis of H_2O_2 from hydrogen (H_2) and oxygen (O_2) is essential for the decentralized production of H_2O_2. Nevertheless, its catalysts usually need precious metals (i.e., Pd and Au), and high concentrations of H_2 and O_2 must be appropriately stored, limiting large-scale practical application (Campos-Martin et al., 2006). Photocatalytic synthesis of H_2O_2 can use unlimited clean solar energy to catalyze the reaction. However, photocatalysts generally suffer from severe photo-corrosion, a high electron-hole recombination rate, slow reaction kinetics, and a narrow absorption wavelength range (Trzciński et al., 2019; Vo et al., 2019; Han et al., 2022). Electrosynthesis of H_2O_2 has significant advantages, such as simple equipment, a controllable production scale, and mild technological conditions. Moreover, it uses electricity from sustainable energy sources and H_2O and O_2 as raw materials, and the production process is 'green' and harmless (Shi et al., 2021).

✉ Chaolin LI, lichaolin@hit.edu.cn
Wenhui WANG, wangwenhui@hit.edu.cn

Chen LING, https://orcid.org/0000-0003-1946-7252
Chaolin LI, https://orcid.org/0000-0001-6059-6836
Wenhui WANG, https://orcid.org/0000-0002-2449-619X

Received Nov. 27, 2022; Revision accepted Jan. 23, 2023;
Crosschecked Feb. 20, 2023; Online first Mar. 23, 2023

Therefore, it has attracted much attention as a promising decentralized production method for practical application.

There are two methods for electrosynthesis of H_2O_2: the two-electron oxygen reduction reaction (2e-ORR, Eq. (1)) and the two-electron water oxidation reaction (2e-WOR, Eq. (2)). For the 2e-ORR, precious metals (i.e., Pd, Au, and Ag) and their alloys (i.e., Pt-Hg) are currently the most advanced catalysts (Siahrostami et al., 2013; Wen et al., 2022), but the scarcity of precious metals may hinder their large-scale application. Some carbon-based materials are seen as potential catalysts for the electrosynthesis of H_2O_2 because they are abundant on earth, have elastic properties, and can operate stably under reactive conditions (Lu et al., 2018). Recently, a natural air-diffused cathode (NADE) loaded with polytetrafluoroethylene/carbon black (PTFE/CB) was reported to achieve efficient 2e-ORR without aeration, thereby advancing the practical application of H_2O_2 electrosynthesis (Zhang et al., 2020). For the 2e-WOR, the efficient electrosynthesis of H_2O_2 is more challenging than for the 2e-ORR because the competitive oxygen evolution reaction (OER, Eq. (3)) has a much lower thermodynamic potential, making H_2O oxidization more prone to OER.

$$O_2 + 2H^+ + 2e^- \rightarrow H_2O_2, \quad E = 0.67\ \text{V}, \tag{1}$$

versus standard hydrogen electrode (SHE):

$$2H_2O \rightarrow H_2O_2 + 2H^+ + 2e^-, \quad E = 1.76\ \text{V vs. SHE}, \tag{2}$$

$$2H_2O \rightarrow O_2 + 4H^+ + 4e^-, \quad E = 1.23\ \text{V vs. SHE}. \tag{3}$$

Previous work on 2e-WOR has focused on screening catalytic materials with appropriate electronic structures, such as the wideband gap metal oxides ZnO (Kelly et al., 2019), WO_3 (Shi et al., 2017), SnO_2 (Fan et al., 2022), TiO_2 (Fuku et al., 2016), $BiVO_4$ (Shi et al., 2018), and $CaSnO_3$ (Park et al., 2019), and carbon-based materials boron-doped diamond (BDD) (Mavrikis et al., 2021) and PTFE modified carbon fiber paper (CFP) (Xia et al., 2020). Although these catalysts have significantly improved H_2O_2 selectivity, viable 2e-WOR catalysts have yet to be developed.

Molecular self-assembly monolayers (SAMs) are 2D structures spontaneously formed by SAM molecules on the surface of solid substrates. They have the advantages of being highly ordered with a uniform arrangement, low surface defects, and a 'crystalline state' (Schwartz, 2001). SAMs are widely used for the surface functionalization of substrate materials. The modification of SAMs is expected to improve the 2e-WOR performance by modulating the microenvironment around the active site of 2e-WOR. However, SAM modification has not been used in the 2e-WOR. Furthermore, note that while the theoretical current efficiency of 2e-WOR or 2e-ORR alone is 100%, if the two methods were combined, the theoretical current efficiency can be doubled. However, the simultaneous electrosynthesis of H_2O_2 via 2e-WOR and 2e-ORR has rarely been reported (Shi et al., 2018; Xia et al., 2020; Li et al., 2022). Herein, we propose a method to modulate the microenvironment around the active site of the 2e-WOR by modifying CFP with SAMs to promote 2e-WOR performance. Also, an NADE was well prepared to combine with the modified anode to further improve the current efficiency, leading to an efficient electrosynthesis of hydrogen peroxide. The coupled functional anode and the prepared NADE can achieve a current efficiency of 152.9%, which is far beyond that of either cathode or anode alone. This work provides a reference for the simultaneous production of H_2O_2 by a cathode and anode.

2 Methods

2.1 Preparation of SAM modified CFP

CFP (thickness of 0.19 mm, Shanghai Hesen Electric Co., Ltd., China) was cut into 1 cm×2 cm pieces and sonicated clean in 10% (mass fraction) HCl solution (36%–38%, HUSHI, China), 10% (mass fraction) NaOH solution (>96%, HUSHI, China), absolute ethanol (>99.5% Macklin, China), acetone (99.5%, HUSHI, China), and deionized water to remove oil and impurities from the surface. The cleaned CFP was oxidized in concentrated HNO_3 (65%, HUSHI, China) at 60 ℃ for 3 h to introduce oxygen-containing functional groups (i.e., –OH and –COOH) on its surface as anchor sites for head groups of the SAM molecules. Subsequently, the oxidized CFP was thoroughly cleaned and dried overnight in a vacuum oven at 60 ℃. Then, the dried CFP was placed vertically in a 50-mL Teflon reactor with a 1-mL glass vial containing 100 μL of 3-mercaptopropyltriethoxysilane ($C_6H_{16}O_3SSi$, MPTES, 97%, Macklin, China). MPTES is a kind of SAM

with a carbon chain structure and –SH as the functional group (Fig. S1 in the electronic supplementary materials). The reactor was filled with argon, sealed within a stainless steel shell, placed in an oven, heated to the specified temperature (140–190 ℃) for 1–8 h, and then naturally cooled to room temperature (about 25 ℃). Finally, the modified CFP was taken out of the reactor and dried in a vacuum oven at 60 ℃. The optimum process conditions were determined as 160 ℃ and 2 h by evaluating the H_2O_2 selectivity (Fig. S2).

2.2 Preparation of NADE

The carbon cloth (CC, thickness of 0.3 mm, Shanghai Hesen Electric Co., Ltd., China) was immersed in 2% (mass fraction) PTFE dispersion (60%, Macklin, China) for 10 min, then removed and dried in an oven at 80 ℃ for 2 h. The dried CC was annealed in a muffle furnace at 350 ℃ for 30 min to obtain the PTFE-treated CC. CB (Ketjen black ECP-600JD, Kelude, China) and PTFE (60%, mass fraction, Macklin, China) were mixed at a mass ratio of 0.2–1.0, then 0.5–1.0 mL absolute ethanol (>99.5%, Macklin, China) was added, and stirred for 2 h to obtain the sizing agent. The sizing agent was evenly coated on the PTFE-treated CC, which was then put into an oven to dry overnight at 80 ℃. Finally, the dried electrodes were annealed at 350 ℃ for 30 min to obtain the NADE.

2.3 Electrosynthesis of H_2O_2

Electrochemical tests were performed in a customized electrolyzer with electrodes separated by a Nafion 117 membrane. All potentials were calibrated with reversible hydrogen electrodes (RHE) ($E_{RHE}=E_{Ag/AgCl}+0.0591\times pH$) without internal resistance compensation (IR compensation). MPTES-modified CFP was used as an anode, NADE as a cathode, and Ag/AgCl (3.5 mol/L KCl) as reference electrodes. The sizes of the anode and cathode immersed in the electrolyte were 1 cm×1 cm and 2 cm×2 cm, respectively. Linear sweep voltammetry (LSV) tests were performed at a scanning rate of 5 mV/s. The frequency range of electrochemical impedance spectroscopy (EIS) was 100 kHz–0.01 Hz with an amplitude of 5 mV. The electrochemical surface area (ECSA) was calculated using the Parsons-Zobel diagram. Cyclic voltammetry was performed at a scanning rate of 10–60 mV/s in a potential of 0.1–0.2 V (vs. Ag/AgCl) to measure double-layer capacitance (Cdl) of different electrodes. The normalized value of ECSA was 24 μF/cm (Xia et al., 2020).

The H_2O_2 selectivity is the ratio of the number of electrons transferred by the formation of H_2O_2 to the total number of electrons transferred. Here, the H_2O_2 selectivity of 2e-WOR or 2e-ORR is expressed as the current efficiency of H_2O_2 produced in a short time. The reaction was terminated when the passing charge reached 10 C or the reaction time reached 10 min. The H_2O_2 concentration was determined by titanium potassium oxalate spectrophotometry. The absorbance value of the complex formed by titanium potassium oxalate and H_2O_2 shows an excellent linear relationship with the H_2O_2 concentration at 400 nm. The Faraday current efficiency (FE) was calculated by the following equation:

$$FE=2CF/Q\times100\%, \tag{4}$$

where C is the amount of generated H_2O_2, mol, F is the Faraday constant, 96485.33 C/mol, and Q is the total amount of charge passed, C.

All experiments were carried out at room temperature. Error bars for experimental results are based on three independent measurements.

2.4 Characterization

Scanning electron microscope (SEM) and energy dispersive spectrometer (EDS) images were collected on a TESCAN MIRA LMS with acceleration voltages of 200 V–30 kV. The droplet contact angles were measured on an OCA20 (Dataphysics, Germany) meter with a droplet of Na_2CO_3 solution. Attenuated total internal reflectance Fourier transform infrared spectroscopy (ATR-FTIR) was performed on a Niolet iN10 (ThermoFisher Scientific, USA) microscope at a wavelength of 600–4000 cm^{-1} to identify the chemical bonds on the electrodes. Raman spectra were acquired on a Alpha300R (WITec, Germany) confocal Raman microscope. The signal was excited by a 532 nm Ventus VIS laser (Laser Quantum, UK), acquired by a ×20 objective, with a dispersion grating of 300 g/mm, and a total of 10 scans were recorded. X-ray photoelectric spectrometry (XPS) was performed on a Nexsa spectrometer (Thermo Scientific, USA) using Al Kα radiation and C 1s (284.8 eV) as a reference value for correcting binding energy.

3 Results and discussion

3.1 Characterization of MPTES-modified CFP

The SEM was used to observe the surface morphology of MPTES modified CFP (S-CFP). Fig. 1a shows that S-CFP preserves the porous structure of CFP (Fig. S3). The spherical particles on the fiber surface are polymers produced by the self-polymerization of MPTES molecules at high temperatures. S and Si elements appear on the S-CFP and are evenly distributed on its surface, which indicates that MPTES successfully grew on the CFP. Fig. 1b shows that the pristine CFP surface is hydrophobic with a contact angle of 115.2°. After oxidation, the contact angle decreased to 33.5° due to the introduction of hydrophilic oxygen-containing functional groups, while the contact angle increased to 138.7° after MPTES modification. These results again suggest that MPTES was successfully grown on the surface of the CFP.

The chemical environment of S-CFP was characterized by Raman spectroscopy (Fig. 1c). The results show that S-CFP had a typical sp^2 carbon structure, with two G peaks around 1582 cm^{-1} and 2700 cm^{-1}, respectively, and an I_D/I_G of 1.35. The increased I_D/I_G compared with pristine CFP (0.03) indicates the increased disorder of the electrodes, which further confirms the successful modification of MPTES. The G-band of S-CFP was wider and shifted toward a higher Raman shift, indicating a symmetry breakdown and

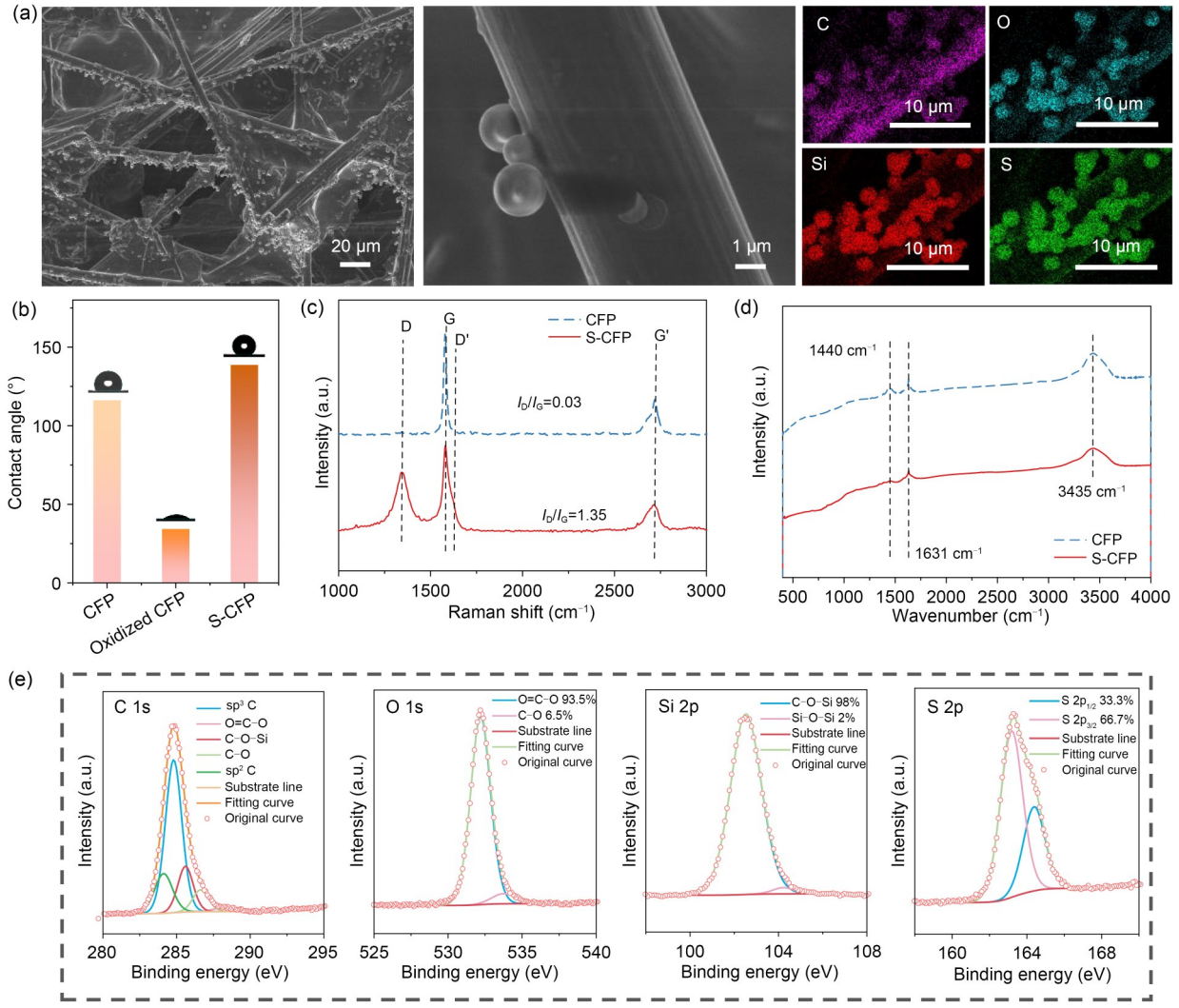

Fig. 1 SEM images and EDS images of S-CFP (a); droplet contact angle images on pristine CFP, oxidized CFP, and S-CFP (b); Raman spectra (c); FTIR spectra (d); high-resolution XPS spectra of S-CFP (e). References to color refer to the online version of this figure

bond deformation, possibly related to the formation of functional groups on the CFP (Papiya et al., 2019).

FTIR was used to identify the functional groups formed on the S-CFP. As shown in Fig. 1d, the stretching vibrations of the OH groups (3435 cm^{-1}) (Fang et al., 2014), the C=C stretching vibration from sp^2 hybridized carbon (1631 cm^{-1}) (Varga et al., 2017), and the bending vibrations of sp^3 hybridized CH_2 (1440 cm^{-1}) (Arbab and Zeinolebadi, 2013) are visible for all electrodes.

XPS spectra were recorded to further confirm the chemical bonds on the electrodes (Fig. 1e). After MPTES modification, the electrode contained 6.6% S and 12.6% Si (Fig. S4). The fitting peaks in the C 1s fine spectrum were 284.1 eV for sp^2 C, 284.8 eV for sp^3 C, 285.7 eV for C–O–Si, 286.7 eV for C–O, and 288.4 eV for O=C–O (Castillo et al., 2016). The O 1s fine spectrum can be deconvoluted into O=C–O at about 532.3 eV and C–O at 533.2 eV (Zhong et al., 2013; Han et al., 2022). The O/C ratio on the electrodes increased from 5.3% in pristine CFP to 37.2% in S-CFP due to the MPTES modification. The Si 2p fine spectrum can be deconvolved into C–O–Si at 102.5 eV and Si–O–Si at 104.3 eV (Sosa et al., 2020). The fitting peaks at 163.2 eV and 164 eV belong to S $2p_{3/2}$ and S $2p_{1/2}$, respectively. The fitting peaks for C–O–Si (285.7 eV and 102.5 eV) and O=C–O suggest that MPTES molecules may form C–O–Si and COOSi on the surface of CFP.

3.2 Electrosynthesis of H_2O_2 via 2e-WOR

A series of electrochemical tests were performed to evaluate the 2e-WOR performance of S-CFP. As shown in Fig. 2a, the activity of S-CFP was significantly increased compared with that of pristine CFP (the original LSV data are shown in Fig. S6). Fig. 2b shows that the electron transfer rate of S-CFP was slower than that of pristine CFP because MPTES molecules self-polymerized to form polymers on the S-CFP that blocked the contact between the active sites and the electrolyte. Even so, the 2e-WOR performance of S-CFP was much higher than that of pristine CFP. As shown in Figs. 2c and 2d, the production rate and selectivity of H_2O_2 were significantly increased after

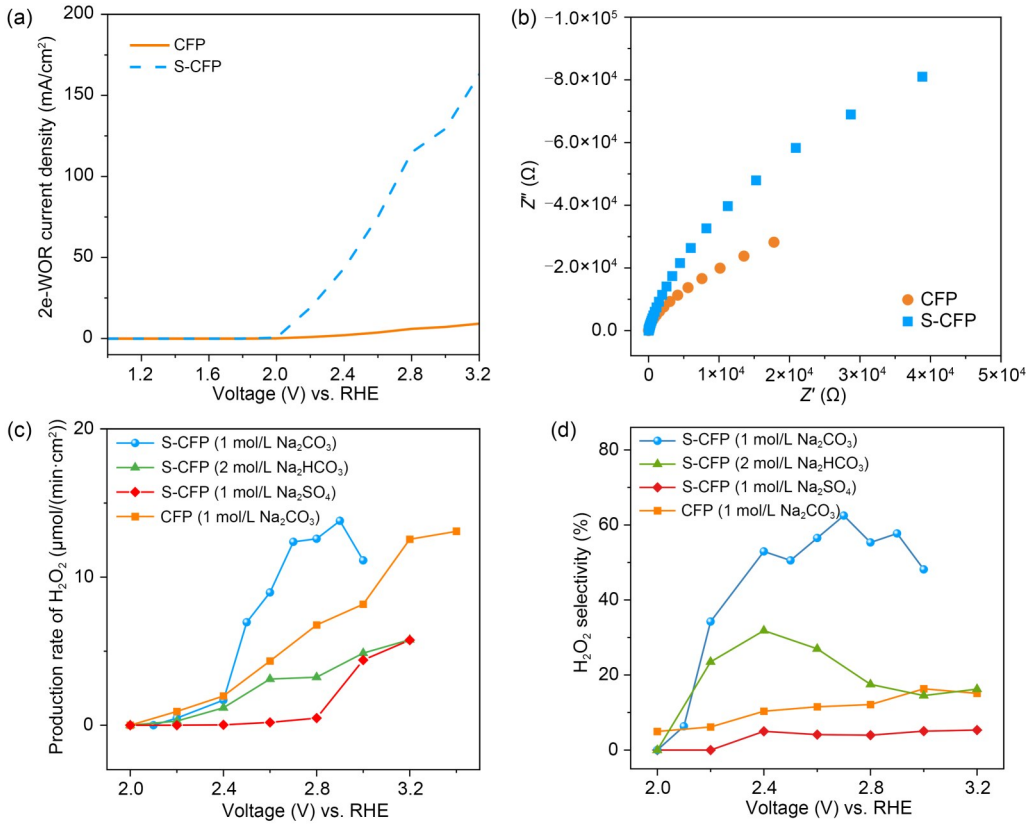

Fig. 2 ECSA normalized 2e-WOR current density (a); EIS of S-CFP and pristine CFP in 1 mol/L Na_2CO_3 solution (b); production rate of H_2O_2 (c); H_2O_2 selectivity of S-CFP and pristine CFP in different electrolytes (d)

MPTES modification, reaching 12.6 μmol/(min·cm^2) and 62.1% at 2.7 V, respectively. In comparison, the production rate and selectivity of H_2O_2 for pristine CFP at the same voltage were only 6.8 μmol/(min·cm^2) and 12.1%, respectively. These results suggest that the chemical bond formed between MPTES and CFP can modulate the active sites to favor the 2e-WOR.

In addition, we found that the type of electrolyte influenced the 2e-WOR performance of S-CFP (Figs. 2c and 2d). S-CFP had a higher selectivity and production rate of H_2O_2 in Na_2CO_3 solution and $NaHCO_3$ solution than that in Na_2SO_4 solution. This may be because CO_3^{2-}/HCO^{3-} can be oxidized to $C_2O_6^{2-}$/HCO_4^- and then hydrolyzed to produce H_2O_2 in the electrolysis process (Eqs. (5) and (6)) (Pangotra et al., 2022). Considering that the 2e-WOR performance of S-CFP in Na_2CO_3 solution was better than that in $NaHCO_3$ solution, the hydrolysis of $C_2O_6^{2-}$ may be the main pathway for H_2O_2 production. Thus, the electrosynthesis mechanism of H_2O_2 in carbonate electrolytes may be similar to that of persulfate in sulfate electrolytes, both of which are oxidizing anions to form corresponding peroxides followed by hydrolysis (Yang et al., 2018). Inspired by this insight, we tried to improve the 2e-WOR performance of S-CFP by using inhibitors of OER, which are widely applied in the electrosynthesis of persulfate (Luo et al., 2017). Fig. S7 shows that KSCN with the concentration of 0.5 mmol/L had the best effect, with H_2O_2 selectivity increasing from 62.1% to 65.9% at 2.7 V. Interestingly, the same phenomenon can be found with Ti_4O_7, Sb-SnO_2, Ru-Ir, and PbO_2, indicating the universality of using KSCN to inhibit OER to improve the 2e-WOR performance of electrodes.

$$HCO_4^- + H_2O \rightarrow H_2O_2 + HCO_3^-, \quad (5)$$

$$C_2O_6^{2-} + 2H_2O \rightarrow H_2O_2 + 2HCO_3^-. \quad (6)$$

3.3 Electrosynthesis of H_2O_2 via 2e-ORR

To combine 2e-WOR with 2e-ORR for simultaneous electrosynthesis of H_2O_2, a NADE was prepared. A NADE provides the O_2 for 2e-ORR by natural air-diffusion without artificial aeration, which is more energy efficient than conventional gas diffusion cathodes. First, the effect of three different substrate materials (i.e., titanium mesh, carbon felt, and CC) used for the NADE was evaluated based on H_2O_2 selectivity. The NADE had the highest H_2O_2 selectivity when CC was used as the substrate (Fig. S8). Then, a series of NADE loaded with different PTFE/CB ratios using CC as substrate were prepared to obtain the best material ratio. LSV tests were performed to reveal the activity of the electrodes. Fig. 3a shows that the NADE with a PTFE/CB ratio of 0.6 had the highest activity, and the activity trend was the same as the ECSA of the NADE (Fig. 3b). This is reasonable considering that the hydrophobicity of electrodes with a low PTFE load (i.e., PTFE/CB=0.2) is insufficient to provide the abundant three-phase interface for 2e-ORR. The electron transport channel is blocked and the electrode activity is reduced when the PTFE content is too high (i.e., PTFE/CB=1). EIS results suggest that the NADE with a PTFE/CB ratio of 0.6 delivered the lowest charge transfer resistance, and the trend was the same as those of the ECSA and LSV tests (Fig. 3c). The H_2O_2 selectivity of different NADEs was measured at current densities ranging at 0–120 mA/cm^2. The NADE with a PTFE/CB ratio of 0.6 had the highest H_2O_2 selectivity, close to 100% at 120 mA/cm^2 (Fig. 3d), which corresponds well to results from the previous electrochemical characterization.

3.4 Electrosynthesis of H_2O_2 via coupling 2e-WOR and 2e-ORR

The S-CFP was combined with the NADE to significantly improve the Faraday current efficiency and the production rate of H_2O_2. Firstly, the performance of simultaneous H_2O_2 electrosynthesis using an anode and cathode in a membrane-free system was evaluated. As shown in Fig. 4a, the total current efficiency of H_2O_2 electrosynthesis increased continuously with the increase of Na_2CO_3 concentration. This was because the amount of H_2O_2 generated via 2e-WOR is highly dependent on carbonate, as revealed in Section 3.1. The total current efficiency reached 136% in 1 mol/L Na_2CO_3 solution, which is much lower than the sum of the respective H_2O_2 selectivity of S-CFP and NADE. The low current efficiency may be related to the mutual interference between the cathode and the anode, thus the proton exchange membrane Nafion 117 was used to address this problem. As expected, the total current efficiency of the system was greatly improved when a divided cell was used. The current efficiency and production rate of H_2O_2 reached 152.9% and 38 μmol/min at 2.8 V, respectively (Figs. 4b and 4c), which is very competitive compared with state-of-the-art literature (Table 1).

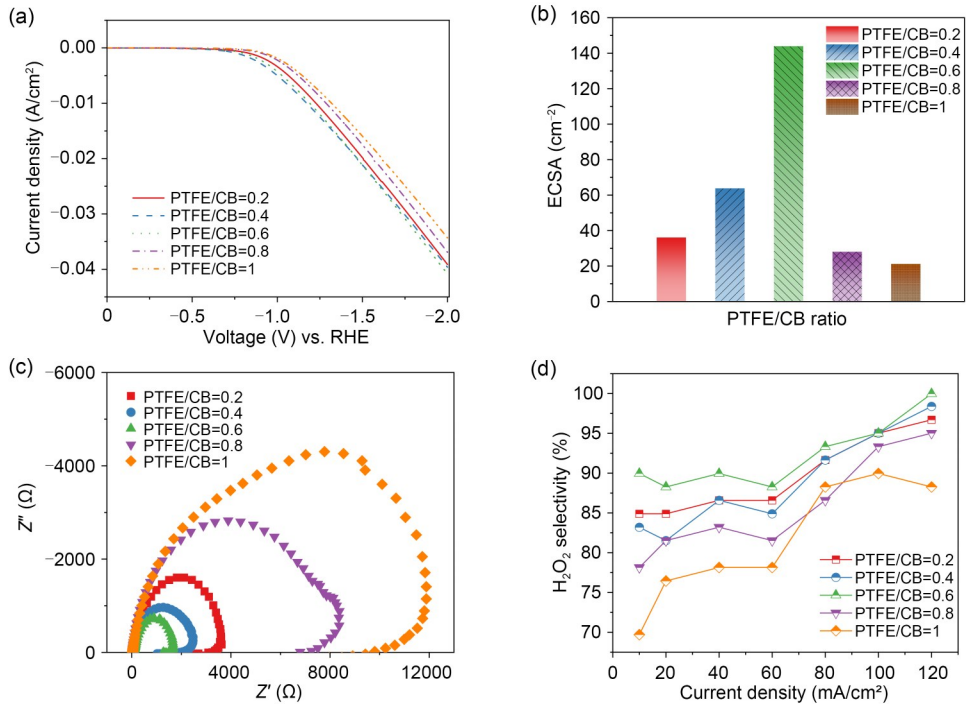

Fig. 3 LSV curves (a), ECSA (b), EIS (c), and H_2O_2 selectivity (d) of NADE with different PTFE/CB ratios in 0.2-mol/L Na_2SO_4 solution

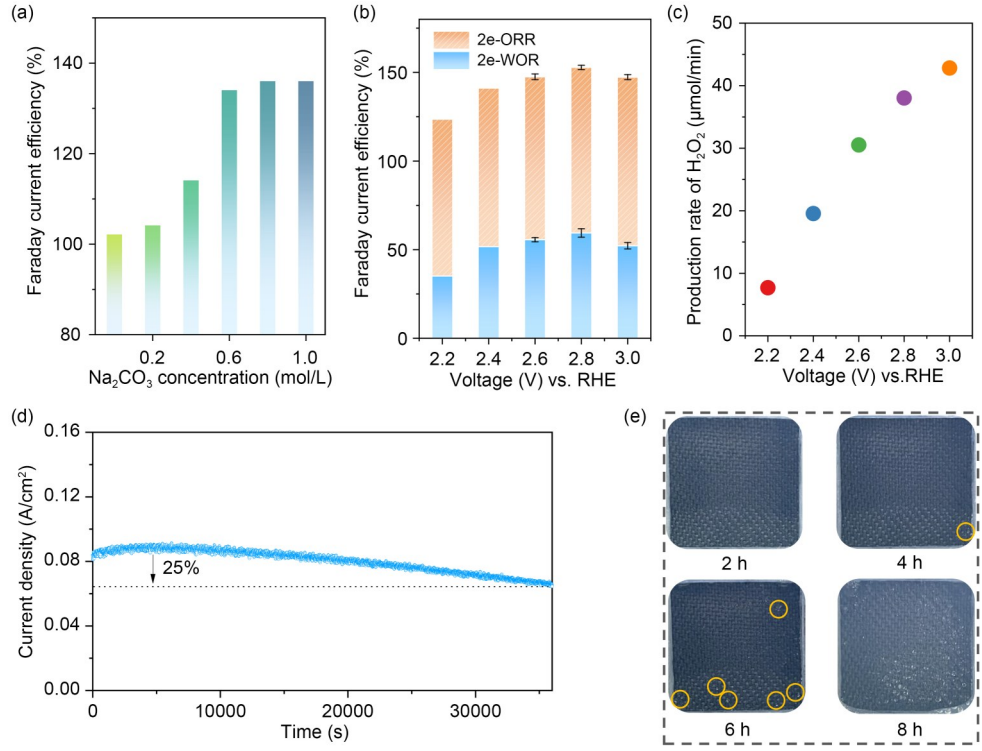

Fig. 4 Total current efficiency of S-CFP and NADE in 0.2-mol/L Na_2SO_4 solution with different Na_2CO_3 contents in a membrane-free electrolyzer (a); total current efficiency (b); the production rate of H_2O_2 of S-CFP and NADE at different voltages in a Nafion 117 membrane-separated electrolyzer (the electrolyte was 1-mol/L Na_2CO_3 in the anode chamber and 0.2-mol/L Na_2SO_4 in the cathode chamber) (c); stability test of S-CFP (d); digital photos of the NADE running for different periods of time (e)

Table 1 Summary of recent studies on the simultaneous production of H_2O_2 by an anode and cathode

Electrode material		Bias applied/ current density	H_2O_2 generation (μmol/min)	Current efficiency	Reference
Anode	Cathode				
$BiVO_4$	C-cathode	1.5 V photoelectric	2.42	–	Shi et al., 2018
$WO_3/BiVO_4$	Au	Photocatalytic	0.066	140%	Fuku et al., 2017
Sn-doped $CuWO_4$/Sn	NADE	100 mA/cm^2	66	161%	Li et al., 2022
PTFE-CFP	Oxidized carbon nanotubes	Cell voltage of about 1.7 V	24	153%	Xia et al., 2020
S-CFP	NADE	2.8 V	38	152.9%	This work

The low production rate of H_2O_2 (usually lower than about 5 μmol/(min·cm^2) synthesized by a photocatalytic or photoelectric system makes it difficult to meet the needs of practical applications (i.e., $BiVO_4$/C-cathode and $WO_3/BiVO_4$/Au). A traditional submerged cathode requires a constant external supply of oxygen, which is energy-intensive (i.e., PTFE-CFP/oxidized carbon nanotubes). In comparison, the NADE used here uses naturally diffused air as the source of oxygen and does not need an artificial oxygen supplement, thus dramatically reducing energy consumption. Therefore, the coupled S-CFP and NADE system developed in this work has promising application prospects. The H_2O_2 electrosynthesis device could run stably for about 4 h (Fig. 4d) until the NADE was flooded by the electrolyte (Fig. 4e). However, after a simple drying the NADE could then continue to be used with no loss of performance from its initial state (Fig. S10).

4 Conclusions

In this paper, a highly efficient 2e-WOR anode was prepared by modifying CFP with MPTES. An H_2O_2 selectivity of 62.1% and H_2O_2 yield of 12.6 μmol/(min·cm^2) were achieved at 2.7 V. A NADE loaded with PTFE/CB=0.6 using CC as substrate was prepared and combined with S-CFP to produce H_2O_2 simultaneously via coupling 2e-WOR and 2e-ORR. The total current density of the 2e-WOR and 2e-ORR reached 152.9%, and the production rate was as high as 38 μmol/min in a Nafion 117 membrane-separated electrolyzer. These findings represent a new strategy for the electrosynthesis of H_2O_2, promoting the practical application of decentralized electrochemical H_2O_2 production.

Acknowledgments

This work is supported by the National Natural Science Foundation of China (Nos. 52170155 and 52100084).

Author contributions

Chen LING, Chaolin LI, and Wenhui WANG designed the research. Chen LING and Aiping LIANG processed the corresponding data. Chen LING wrote the first draft of the manuscript. Chaolin LI and Wenhui WANG helped to organize the manuscript. Chaolin LI and Wenhui WANG revised and edited the final version. Chaolin LI and Wenhui WANG are the funding acquisition.

Conflict of interest

Chen LING, Aiping LIANG, Chaolin LI, and Wenhui WANG declare that they have no conflict of interest.

References

Arbab S, Zeinolebadi A, 2013. A procedure for precise determination of thermal stabilization reactions in carbon fiber precursors. *Polymer Degradation and Stability*, 98(12): 2537-2545. https://doi.org/10.1016/j.polymdegradstab.2013.09.014

Campos-Martin JM, Blanco-Brieva G, Fierro JLG, 2006. Hydrogen peroxide synthesis: an outlook beyond the anthraquinone process. *Angewandte Chemie International Edition*, 45(42):6962-6984. https://doi.org/10.1002/anie.200503779

Castillo GA, Wilson L, Efimenko K, et al., 2016. Amidation of polyesters is slow in nonaqueous solvents: efficient amidation of poly(ethylene terephthalate) with 3-aminopropyltriethoxysilane in water for generating multifunctional surfaces. *ACS Applied Materials & Interfaces*, 8(51):35641-35649. https://doi.org/10.1021/acsami.6b12155

Edwards JK, Hutchings GJ, 2008. Palladium and gold-palladium catalysts for the direct synthesis of hydrogen peroxide. *Angewandte Chemie International Edition*, 47(48):9192-9198. https://doi.org/10.1002/anie.200802818

Fan L, Bai XW, Xia C, et al., 2022. CO_2/carbonate-mediated electrochemical water oxidation to hydrogen peroxide. *Nature Communications*, 13(1):2668. https://doi.org/10.1038/s41467-022-30251-5

Fang CQ, Wang JL, Zhang T, 2014. Interlaminar improvement of carbon fiber/epoxy composites via depositing mixture of carbon nanotubes and sizing agent. *Applied Surface Science*, 321:1-9. https://doi.org/10.1016/j.apsusc.2014.09.170

Fuku K, Miyase Y, Miseki Y, et al., 2016. Enhanced oxidative

hydrogen peroxide production on conducting glass anodes modified with metal oxides. *ChemistrySelect*, 1(18): 5721-5726. https://doi.org/10.1002/slct.201601469

Fuku K, Miyase Y, Miseki Y, et al., 2017. Photoelectrochemical hydrogen peroxide production from water on a WO_3/$BiVO_4$ photoanode and from O_2 on an Au cathode without external bias. *Chemistry-An Asian Journal*, 12(10): 1111-1119. https://doi.org/10.1002/asia.201700292

Gopakumar A, Ren P, Chen JH, et al., 2022. Lignin-supported heterogeneous photocatalyst for the direct generation of H_2O_2 from seawater. *Journal of the American Chemical Society*, 144(6):2603-2613. https://doi.org/10.1021/jacs.1c10786

Hage R, Lienke A, 2006. Applications of transition-metal catalysts to textile and wood-pulp bleaching. *Angewandte Chemie International Edition*, 45(2):206-222. https://doi.org/10.1002/anie.200500525

Han GW, Xu FY, Cheng B, et al., 2022. Enhanced photocatalytic H_2O_2 production over inverse opal ZnO@polydopamine S-scheme heterojunctions. *Acta Physico-Chimica Sinica*, 38(7):2112037 (in Chinese). https://doi.org/10.3866/pku.whxb202112037

Kelly SR, Shi XJ, Back S, et al., 2019. ZnO as an active and selective catalyst for electrochemical water oxidation to hydrogen peroxide. *ACS Catalysis*, 9(5):4593-4599. https://doi.org/10.1021/acscatal.8b04873

Kosaka K, Yamada H, Shishida K, et al., 2001. Evaluation of the treatment performance of a multistage ozone/hydrogen peroxide process by decomposition by-products. *Water Research*, 35(15):3587-3594. https://doi.org/10.1016/s0043-1354(01)00087-2

Li LJ, Hu ZF, Yu JC, 2020. On-demand synthesis of H_2O_2 by water oxidation for sustainable resource production and organic pollutant degradation. *Angewandte Chemie International Edition*, 59(46):20538-20544. https://doi.org/10.1002/anie.202008031

Li LJ, Xu LP, Chan AWM, et al., 2022. Direct hydrogen peroxide synthesis on a Sn-doped $CuWO_4$/Sn anode and an air-breathing cathode. *Chemistry of Materials*, 34(1):63-71. https://doi.org/10.1021/acs.chemmater.1c02787

Lu ZY, Chen GX, Siahrostami S, et al., 2018. High-efficiency oxygen reduction to hydrogen peroxide catalysed by oxidized carbon materials. *Nature Catalysis*, 1(2):156-162. https://doi.org/10.1038/s41929-017-0017-x

Luo HJ, Li CL, Sun X, et al., 2017. Cathodic indirect oxidation of organic pollutant paired to anodic persulfate production. *Journal of Electroanalytical Chemistry*, 792: 110-116. https://doi.org/10.1016/j.jelechem.2017.03.040

Ma J, Choudhury NA, Sahai Y, 2010. A comprehensive review of direct borohydride fuel cells. *Renewable and Sustainable Energy Reviews*, 14(1):183-199. https://doi.org/10.1016/j.rser.2009.08.002

Mavrikis S, Göltz M, Perry SC, et al., 2021. Effective hydrogen peroxide production from electrochemical water oxidation. *ACS Energy Letters*, 6(7):2369-2377. https://doi.org/10.1021/acsenergylett.1c00904

Pangotra D, Csepei LI, Roth A, et al., 2022. Anodic production of hydrogen peroxide using commercial carbon materials. *Applied Catalysis B: Environmental*, 303:120848. https://doi.org/10.1016/j.apcatb.2021.120848

Papiya F, Das S, Pattanayak P, et al., 2019. The fabrication of silane modified graphene oxide supported Ni-Co bimetallic electrocatalysts: a catalytic system for superior oxygen reduction in microbial fuel cells. *International Journal of Hydrogen Energy*, 44(47):25874-25893. https://doi.org/10.1016/j.ijhydene.2019.08.020

Park SY, Abroshan H, Shi XJ, et al., 2019. $CaSnO_3$: an electrocatalyst for two-electron water oxidation reaction to form H_2O_2. *ACS Energy Letters*, 4(1):352-357. https://doi.org/10.1021/acsenergylett.8b02303

Samanta C, Choudhary VR, 2007. Direct formation of H_2O_2 from H_2 and O_2 and decomposition/hydrogenation of H_2O_2 in aqueous acidic reaction medium over halide-containing Pd/SiO_2 catalytic system. *Catalysis Communications*, 8(12): 2222-2228. https://doi.org/10.1016/j.catcom.2007.05.007

Schwartz DK, 2001. Mechanisms and kinetics of self-assembled monolayer formation. *Annual Review of Physical Chemistry*, 52:107-137. https://doi.org/10.1146/annurev.physchem.52.1.107

Shi XJ, Siahrostami S, Li GL, et al., 2017. Understanding activity trends in electrochemical water oxidation to form hydrogen peroxide. *Nature Communications*, 8(1):701. https://doi.org/10.1038/s41467-017-00585-6

Shi XJ, Zhang YR, Siahrostami S, et al., 2018. Light-driven $BiVO_4$-C fuel cell with simultaneous production of H_2O_2. *Advanced Energy Materials*, 8(23):1801158. https://doi.org/10.1002/aenm.201801158

Shi XJ, Back S, Gill TM, et al., 2021. Electrochemical synthesis of H_2O_2 by two-electron water oxidation reaction. *Chem*, 7(1):38-63. https://doi.org/10.1016/j.chempr.2020.09.013

Siahrostami S, Verdaguer-Casadevall A, Karamad M, et al., 2013. Enabling direct H_2O_2 production through rational electrocatalyst design. *Nature Materials*, 12(12):1137-1143. https://doi.org/10.1038/nmat3795

Sosa N, Chanlek N, Wittayakun J, 2020. Facile ultrasound-assisted grafting of silica gel by aminopropyltriethoxysilane for aldol condensation of furfural and acetone. *Ultrasonics Sonochemistry*, 62:104857. https://doi.org/10.1016/j.ultsonch.2019.104857

Tanev PT, Chibwe M, Pinnavaia TJ, 1994. Titanium-containing mesoporous molecular sieves for catalytic oxidation of aromatic compounds. *Nature*, 368(6469):321-323. https://doi.org/10.1038/368321a0

Trzciński K, Szkoda M, Szulc K, et al., 2019. The bismuth vanadate thin layers modified by cobalt hexacyanocobaltate as visible-light active photoanodes for photoelectrochemical water oxidation. *Electrochimica Acta*, 295: 410-417. https://doi.org/10.1016/j.electacta.2018.10.167

Varga M, Izak T, Vretenar V, et al., 2017. Diamond/carbon

nanotube composites: Raman, FTIR and XPS spectroscopic studies. *Carbon*, 111:54-61. https://doi.org/10.1016/j.carbon.2016.09.064

Vo TG, Tai Y, Chiang CY, 2019. Novel hierarchical ferric phosphate/bismuth vanadate nanocactus for highly efficient and stable solar water splitting. *Applied Catalysis B: Environmental*, 243:657-666. https://doi.org/10.1016/j.apcatb.2018.11.001

Wen FC, Li SRGG, Chen Y, et al., 2022. Corrugated rGO-supported Pd composite on carbon paper for efficient cathode of Mg-H_2O_2 semi-fuel cell. *Rare Metals*, 41(8): 2655-2663. https://doi.org/10.1007/s12598-022-01964-9

Xia C, Back S, Ringe S, et al., 2020. Confined local oxygen gas promotes electrochemical water oxidation to hydrogen peroxide. *Nature Catalysis*, 3(2):125-134. https://doi.org/10.1038/s41929-019-0402-8

Yang SQ, Cui YH, Liu YY, et al., 2018. Electrochemical generation of persulfate and its performance on 4-bromophenol treatment. *Separation and Purification Technology*, 207: 461-469. https://doi.org/10.1016/j.seppur.2018.06.071

Zhang QZ, Zhou MH, Ren GB, et al., 2020. Highly efficient electrosynthesis of hydrogen peroxide on a superhydrophobic three-phase interface by natural air diffusion. *Nature Communications*, 11(1):1731. https://doi.org/10.1038/s41467-020-15597-y

Zhong RS, Qin YH, Niu DF, et al., 2013. Effect of carbon nanofiber surface functional groups on oxygen reduction in alkaline solution. *Journal of Power Sources*, 225:192-199. https://doi.org/10.1016/j.jpowsour.2012.10.043

Electronic supplementary materials

Figs. S1–S10